# Optical spectroscopy and decoherence studies of $Yb^{3+}$:YAG at 968 nm

Thomas Böttger*
*Department of Physics and Astronomy, University of San Francisco, 2130 Fulton Street, San Francisco, California 94117, USA*

C. W. Thiel† and R. L. Cone
*Department of Physics, Montana State University, Bozeman, Montana 59717, USA*

Y. Sun
*Department of Physics, University of South Dakota, Vermillion, South Dakota 57069, and Department of Physics, Montana State University, Bozeman, Montana 59717, USA*

A. Faraon
*T. J. Watson Laboratory of Applied Physics, California Institute of Technology, 1200 E. California Boulevard, Pasadena, California 91125, USA*

(Received 24 March 2016; revised manuscript received 27 June 2016; published 26 July 2016)

The $^2F_{7/2} \leftrightarrow {}^2F_{5/2}$ optical transitions of $Yb^{3+}$ doped into $Y_3Al_5O_{12}$ (YAG) were studied for potential quantum information and photonic signal processing applications. Absorption and fluorescence spectroscopy located the energy levels of the ground $^2F_{7/2}$ and excited $^2F_{5/2}$ manifolds, allowing inconsistencies between previous assignments of crystal field splittings in the literature to be resolved. These measurements reveal an unusually large splitting between the first and second levels in both the ground and excited multiplets, potentially providing for reduced sensitivity to thermally induced decoherence and spin-lattice relaxation. Spectral hole burning through two-level saturation was observed, determining the excited state lifetime to be 860 $\mu$s and resolving ambiguities in previous fluorescence measurements that were caused by the large radiation trapping effects in this material. Optical decoherence measurements using two-pulse photon echoes gave a homogeneous linewidth of 18 kHz for an applied magnetic field of 1 T, narrowing to 5 kHz at 2.5 T. The observed decoherence was described by spectral diffusion attributed to $Yb^{3+}$-$Yb^{3+}$ magnetic dipole interactions. Laser absorption determined an inhomogeneous linewidth of 3.6 GHz for this transition in this 0.05%-doped crystal, which is narrower than for any other rare-earth-ion transition previously studied in the YAG host. The temperature dependence of the transition energy and linewidth of the lowest $^2F_{7/2}$ to lowest $^2F_{5/2}$ transition centered at 968.571 nm measured from 4 K to 300 K was well described by phonon scattering at higher temperatures, with an additional anomalous linear temperature-dependent broadening at temperatures below 80 K. Two magnetically inequivalent subgroups of $Yb^{3+}$ ions were identified when a magnetic field was applied along the $\langle 111 \rangle$ axis, as expected for the $D_2$ sites in the cubic symmetry crystal, with ground and excited state effective $g$-values of $g_g = 3.40$ (3.34) and $g_e = 1.04$ (2.01), respectively. Together with the convenient diode laser wavelength of this transition, our study suggests that $Yb^{3+}$:YAG is a promising material system for spectral hole burning and quantum information applications.

DOI: 10.1103/PhysRevB.94.045134

## I. INTRODUCTION

Rare-earth-doped materials at cryogenic temperatures have become very attractive active material systems in the quest to build practical quantum memory and optical signal processing devices [1–4]. In the rapidly developing field of quantum information science (QIS), the unique material properties offered by these materials are exploited to process, store, and transmit data in ways that are unprecedented and moreover are impossible with classical computing. Extensive material research, however, is necessary to fully understand the capabilities and limitations of each material system and to provide the range of material systems, having complementary properties, required to enable different applications.

The paramagnetic $Yb^{3+}$ ion offers optical transitions near 1 $\mu$m suitable for spectral hole burning and well matched to commercial diode lasers [5]. While the optical coherence properties of these transitions to our knowledge have not been studied previously, we expect many of their properties to be similar to those for the paramagnetic $Er^{3+}$ ion, which has become a key system used in a range of classical signal processing and quantum information demonstrations.

The material studied here, yttrium aluminum garnet $Y_3Al_5O_{12}$ (YAG) doped with $Yb^{3+}$, is widely known for its extensive use in high-power diode-pumped solid-state lasers [6–8], where it replaces Nd:YAG systems in many applications [9], and in high-power optical amplifiers [10]. In this context, $Yb^{3+}$:YAG has favorable material characteristics such as a large absorption bandwidth, a long upper-level radiative lifetime, a small quantum defect, no excited state absorption or up-conversion losses, and high thermal conductivity. In addition, large high-quality single crystals of YAG can be grown with high concentrations of $Yb^{3+}$ dopant ions.

*Corresponding author: tbottger@usfca.edu
†Corresponding author: thiel@physics.montana.edu

 

Ytterbium-doped materials are very interesting for applications in QIS, such as for on-chip optical quantum memories [1,2,11–13] and quantum transducers between optical photons and microwave photons [14,15]. The primary advantage of the $Yb^{3+}$-doped system for quantum memory is the operating wavelength in the near infrared because it is easily accessible with laser diodes. Also, the $^{171}Yb$ isotope has a nuclear spin of $I = 1/2$, giving one of the simplest hyperfine level structures for all of the Kramers ions; this makes it very attractive for applications in optical to microwave quantum conversion, where microwave photons are coupled to the hyperfine transitions in the ground state manifold.

To our knowledge, in the area of spectral hole burning (SHB) and QIS applications, $Yb^{3+}$:YAG has not been investigated. Only a few moderately high-resolution spectroscopy studies have been carried out [16–25], with conflicting results, so that basic properties such as assignment of energy levels for the $D_2$ symmetry $Yb^{3+}$ sites remain uncertain [23].

In the work reported here, we apply a wide variety of optical techniques to determine fundamental material parameters such as transition frequencies, energy level structure, excited state population dynamics, ground and excited state Zeeman effects, and optical decoherence as a function of temperature from 4 K to 300 K. These results indicate that $Yb^{3+}$:YAG is a promising system for SHB applications, suggesting broad applications for this material beyond solid-state lasers.

The paper is organized into several sections as follows. Section II describes the general material properties of $Yb^{3+}$:YAG, while Sec. III provides a detailed account of all experimental setups for the different spectroscopic measurements. In the main Sec. IV, we present results and discussion of the spectroscopic properties for the $^2F_{7/2} \leftrightarrow {}^2F_{5/2}$ transition of $Yb^{3+}$:YAG. This particular section is organized into subsections A (Absorption and Fluorescence Spectra of the $^2F_{7/2} \leftrightarrow {}^2F_{5/2}$ Transition), B (High-Resolution Laser-Absorption Spectrum of the $^2F_{7/2} \leftrightarrow {}^2F_{5/2}$ Transition), C (Characterization of the Zeeman Effect), D (Thermal Shift of the Transition Energy), E (Temperature Dependence of the Homogeneous Linewidth), F (Fluorescence Lifetime Measurements), G (Spectral Hole Burning and Spectral Hole Decay Measurements), and H (Probing Optical Decoherence as a Function of Magnetic Field Strength).

## II. $Yb^{3+}$:YAG MATERIAL PROPERTIES

All $Yb^{3+}$:YAG crystals used in this study were grown by Scientific Materials Corp. (Bozeman, Montana) by the Czochralski method. The crystal boules were pulled from the melt along the crystallographic ⟨111⟩ direction, and cross-sectional windows of varying thickness were cut from the boules and polished to optical quality. The $Yb^{3+}$:YAG crystals had nominal $Yb^{3+}$ dopant concentrations of 0.05% (growth no. 2–715) and 1.5% (growth no. 2–523) atomic percent substitution for $Y^{3+}$. All crystals were transparent and appeared colorless. The YAG crystal belongs to the cubic space group $\bar{3}d$ ($O_h^{10}$, #230). The unit cell contains 8 formula units with 160 atoms, and the lattice constant is 12.012Å [26,27]. The $Y^{3+}$ ions occupy a single crystallographic site with local $D_2$ point symmetry and a density of $1.38 \times 10^{22}$ ions $cm^{-3}$, and the $Yb^{3+}$ ions substitute for $Y^{3+}$ host ions without charge compensation [27–29]. The ionic radius of $Yb^{3+}$ ions (0.0985 nm) is only slightly smaller than the ionic radius of $Y^{3+}$ ions (0.1019 nm) [30], and very high $Yb^{3+}$ doping concentrations are possible up to stoichiometric $Yb_3Al_5O_{12}$. For the low $Yb^{3+}$ doping levels used in this study, we expect the majority of $Yb^{3+}$ ions to occupy the unperturbed intrinsic $D_2$ site of the lattice. Small satellite lines adjacent to the main absorption associated with perturbed sites were also observed in the absorption spectra, likely resulting from neighboring Y-Al antisite defects, which are known to occur in the YAG lattice [31–34]. While ytterbium dopants are expected primarily in the trivalent state in YAG due to the size and valence match with $Y^{3+}$, depending on growth and processing conditions, it is also possible for $Yb^{2+}$ ions to be present, resulting in additional lattice strain and an increased concentration of charge compensating defects such as oxygen vacancies. Although $Yb^{2+}$ has a $4f^{14}$ closed electronic shell, optical absorption due to interconfigurational $4f^{14}$ to $4f^{13}5d^1$ and charge transfer transitions cause crystals that contain significant $Yb^{2+}$ to exhibit a pale blue color [35]. All of the crystals used in this work were without any observable coloration.

The ytterbium atom has seven naturally occurring isotopes, with only two having nonzero nuclear spin. The $^{171}Yb$ isotope has a nuclear spin of $I = 1/2$ and a relative natural abundance of 14%, while $^{173}Yb$ has a nuclear spin of $I = 5/2$ and a relative abundance of 16% [36]. In some cases, a nonzero nuclear spin may be desirable to allow for optical pumping of populations between nuclear hyperfine levels. In particular, $^{171}Yb$ is unique in being the only stable isotope of all of the paramagnetic rare-earth ions that has a nuclear spin of $I = 1/2$, providing a particularly simple hyperfine structure that is an advantage for some applications. Thus, depending on the specific requirements of the application, samples with enriched levels of either $^{171}Yb$ or $^{173}Yb$ may be grown.

## III. EXPERIMENT

Absorption spectra were measured to identify the optical transition energies and to quantitatively determine the optical linewidths and absorption coefficients. The transition energy and linewidth of the most important transition from the ground state to the lowest $^2F_{5/2}$ excited state were also measured as a function of temperature. Two 0.05% $Yb^{3+}$:YAG samples with thicknesses of 10 mm and 3.87 mm were mounted in a Cryomech PT405 cryocooler modified by S2 Corp. (Bozeman, Montana) for reduced vibrational motion. The thicker sample was used for the temperature range between 300 K and 150 K, whereas the thinner sample was used between 8 K and 150 K to avoid overabsorption. A tungsten halogen light source (Ocean Optics HL-2000-FHSA) was focused onto the masked sample held in the cryocooler, and the transmitted signal was collected with a multimode optical fiber coupled into an Advantest Q8347 optical spectrum analyzer with a resolution of 0.003 nm (900 MHz). For a broader 80 nm absorption scan at $T = 3$ K, we used an Ando AQ6317B optical spectrum analyzer with a resolution of 0.057 nm.

Zeeman absorption experiments were carried out with a 10-mm-thick 0.05% $Yb^{3+}$:YAG crystal held in an Oxford Spectromag cryostat, allowing measurements as a function

of magnetic field and temperature. For this purpose, the tungsten halogen source was focused onto the masked sample held in the cryostat, and the transmitted signal was collected and refocused onto the entrance slit of a SPEX 1000M monochromator with a bandpass of $0.3\,\mathrm{cm}^{-1}$ at 1000 nm. To observe and identify all possible transitions between the Zeeman-split ground and excited states, data were collected at 2 K and 10 K. The signal was detected with a liquid-nitrogen-cooled Advanced Detector Corporation model C3L germanium detector and then amplified, digitized, and recorded. The absolute frequency of the spectrum was calibrated using a narrowband New Focus Vortex external cavity diode laser (ECDL) as a marker in the spectrum, and frequency was measured with a Burleigh WA-1500 wavemeter.

Fluorescence spectra to map out the ground state multiplet were measured using the same spectrometer arrangement but with a 1.0-mm-thick 0.05% $Yb^{3+}$:YAG sample held in the cryocooler at $T = 4\,\mathrm{K}$. In this case, the ECDL light was propagated with $\mathbf{k} \parallel \langle 110\rangle$ to excite the lowest level of the $^2F_{5/2}$ multiplet at 968.571 nm while continuously scanning over 100 MHz in order to avoid any SHB effects. Fluorescence was collected at an angle of 90° with respect to the laser beam, chopped at a frequency of 500 Hz with a Stanford Research Systems chopper, and focused onto the spectrometer entrance slit. The spectrally filtered fluorescence was detected using the liquid-nitrogen-cooled germanium detector, and the signal was demodulated and filtered by a Princeton Applied Research 5204 lock-in analyzer. The fluorescence excitation wavelength of the ECDL was monitored with the Burleigh WA-1500 wavemeter and provided a marker in the fluorescence spectra for absolute frequency calibration.

To determine an upper limit for the fluorescence lifetime of the metastable $^2F_{5/2}$ state, the output of the ECDL was gated with a 165 MHz acousto-optic modulator (AOM) to produce sharp-edged 50 $\mu$s pulses at a 10 Hz repetition rate, which were used to pump the $^2F_{7/2}$ to $^2F_{5/2}$ absorption. The fluorescence intensity was recorded as a function of time with a liquid-nitrogen-cooled Hamamatsu R3809U-69 near-infrared photomultiplier tube, with the SPEX spectrometer tuned to the lowest to lowest $^2F_{5/2}$ to $^2F_{7/2}$ transition. Measurements were conducted for different temperatures and $Yb^{3+}$ dopant concentrations.

More accurate excited state lifetime measurements were provided by time-resolved SHB. For this measurement, the 1-mm-thick 0.05% $Yb^{3+}$:YAG sample was used and mounted in the cryocooler, with a measured temperature at the sample of $T = 2.8\,\mathrm{K}$. A small magnetic field at the sample was generated using a stack of N50-grade NdFeB permanent magnets mounted outside the cryocooler, providing a field strength of ~20 Gauss at the sample with $\mathbf{B}||\langle 111\rangle$, as measured using a Hall probe and confirmed by Zeeman experiments. The laser light was propagated with $\mathbf{k}||\langle 110\rangle$, and a polarizer and half-wave plate were used to adjust the laser polarization to $\mathbf{E}||\langle 111\rangle$.SHB spectra were obtained with a pump-probe scheme. For this purpose, the laser light was coupled through two 200 MHz AOMs in series to achieve a high contrast and to maintain the laser frequency. The output of the laser was sent through a variable attenuator to allow the intensity at the sample to be controlled. Spectral holes were generated using a burn pulse of 2.5 ms length that was focused into the 1-mm-thick crystal and tuned to the center of the inhomogeneously broadened line. Spectral holes were read out after a time delay varying between 50 $\mu$s and 3.5 ms by applying a chirp pulse to the piezoelectric transducer (PZT) driving the feedback mirror of the ECDL. Typical chirp rates were several megahertz per microsecond. Measuring the hole spectrum as a function of the time delay between burn and readout pulses allowed measurement of the $^2F_{5/2}$ population decay.

High-resolution laser-absorption scans with the ECDL were used to accurately measure the linewidth and wavelength of the strongest line. For this purpose, a 1-mm-thick 0.05% $Yb^{3+}$:YAG sample was held in the cryocooler at a temperature of 3.6 K, and collimated laser light was propagated with $\mathbf{k}||\langle 110\rangle$ through the crystal. The laser-absorption spectra were measured by tuning the laser with the PZT and detecting the transmission through the crystal with a New Focus 1811 InGaAs photodetector. A free-space Fabry-Pérot interferometer spectrum with free spectral range of 96.7 MHz was recorded simultaneously to provide a precise frequency calibration of the scan. Reference transmission spectra without the sample were measured to correct for interference fringes and laser intensity variations. Several laser-absorption scans were averaged to obtain the final spectrum. The absolute frequency of the main absorption line was accurately measured with a Burleigh WA-1500 wavemeter.

Decoherence properties of $Yb^{3+}$:YAG were investigated using two-pulse photon echo decays as a function of magnetic field strength. A 165 MHz acousto-optic modulator gated the laser beam to generate the pulses for echo excitation. The pulse widths were ~2 $\mu$s for the first pulse and ~2.7 $\mu$s for the second pulse. For these experiments, we used a 10-mm-thick 0.05% $Yb^{3+}$:YAG sample. The laser beam was focused inside the crystal held in the Oxford Spectromag cryostat at $T = 1.6\,\mathrm{K}$ with $\mathbf{B}||\langle 111\rangle$. Photon echo signals were detected using a New Focus 1811 InGaAs photodiode and processed with a digital oscilloscope interfaced with a data-acquisition computer.

## IV. SPECTROSCOPIC PROPERTIES OF $Yb^{3+}$:YAG

### A. Absorption and fluorescence spectra of the $^2F_{7/2} \leftrightarrow {}^2F_{5/2}$ transition

The optical transition of interest for SHB and QIS applications employed in $Yb^{3+}$ materials is the transition between the lowest crystal field levels of the $^2F_{7/2}$ and $^2F_{5/2}$ multiplets, which were first measured by Wood at liquid nitrogen temperature of 77 K [16] and at 10 K by Lupei [23]. Figure 1 shows our unpolarized broadband absorption spectrum for 0.05% $Yb^{3+}$:YAG at T = 3 K. The absorption spectrum reveals that the largest absorption coefficient occurs for the desired lowest to lowest $^2F_{7/2}(1) \rightarrow {}^2F_{5/2}(1)$ transition. As expected for the cubic crystal, no polarization dependence was observed. We find the lowest transition to be quite narrow and with an energy of $10\,324.5\,\mathrm{cm}^{-1}$ (968.571 nm in vacuum). This value is slightly different from previously reported values, which have ranged from $10\,321\mathrm{cm}^{-1}$ to $10\,336\,\mathrm{cm}^{-1}$ [16,18–23,25]. If we assume that the previously reported numbers correspond to the inverse of wavelength in ambient air and not in vacuum, our measurements for the low-temperature (<80 K) transition energy agree well with the values given

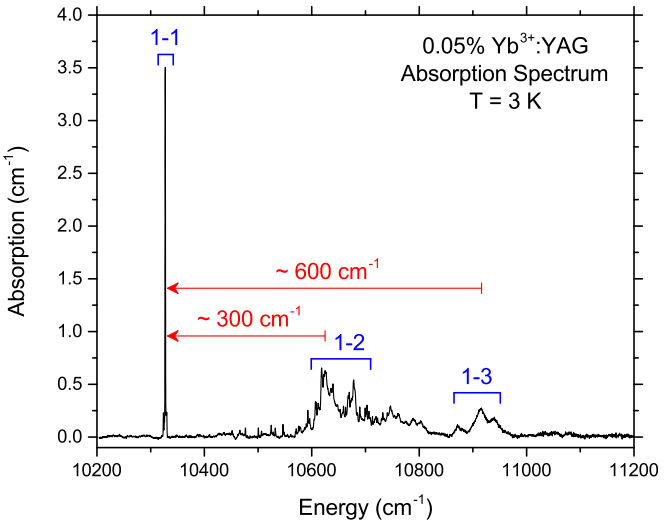


FIG. 1. Absorption spectrum of 0.05% $Yb^{3+}$:YAG (unpolarized) for the $^2F_{7/2}$ to $^2F_{5/2}$ transition at T = 3 K. Indicated are the transitions from the lowest level of $^2F_{7/2}$ (1) to the three Stark levels of $^2F_{5/2}$.

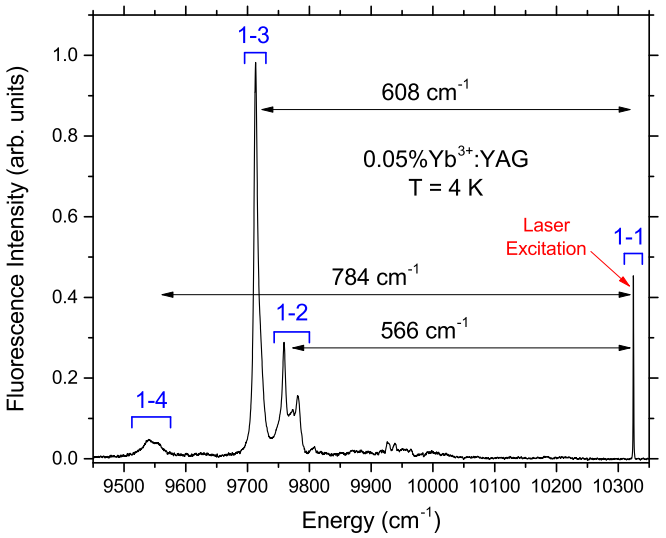


FIG. 2. Fluorescence spectrum of $^2F_{5/2} \rightarrow {}^2F_{7/2}$ for 0.05% $Yb^{3+}$:YAG at T = 4 K. To avoid spectral hole burning, the spectrum was measured by exciting the $^2F_{5/2}$ (1) level at 10 324.5 $cm^{-1}$ with a laser. Energy differences were measured between the peaks of the emission intensity for each transition.

in Refs. [20,22,23,25]. At 300 K, we find that the measured transition energy is 10 321.6 $cm^{-1}$ (968.842 nm in vacuum), which is comparable to the values in Refs. [18,19], if we assume that they give inverse wavelength in air, suggesting that their reported numbers correspond to ambient temperature rather than 77 K as indicated. We should note that the transition shifts to higher energy with increased $Yb^{3+}$ concentration by $\sim$0.07 $cm^{-1}$/at.% [18], causing small changes in the transition energy for higher doping levels.

The observed complex structure of the higher energy transitions is believed to result from a combination of (1) the $1 \rightarrow 2$ and $1 \rightarrow 3$ electronic transitions, (2) vibronic sidebands primarily associated with the $1 \rightarrow 1$ transition [18], (3) additional splittings of the $1 \rightarrow 2$ and $1 \rightarrow 3$ transitions due to near-resonant electron-phonon interactions [23,37], and (4) perturbed $Yb^{3+}$ sites in the crystal [17]. Together, these effects result in the broad distribution of absorption features that overlap with transitions to the second and third Stark levels of the excited $^2F_{5/2}$ multiplet and make definitive assignments difficult [23,38]. Detailed modeling of the experimental data in the framework of first vibronic sidebands by Buchanan *et al.* [18], later expanded and refined by Lupei *et al.* [23] to include additional resonant electron-phonon coupling effects, has allowed the positions of the electronic levels to be estimated. We find that our measured spectrum agrees well with the results of Ref. [38], and the corresponding transitions have been labeled in Fig. 1. We assign the structure at $\sim$300$cm^{-1}$ above the lowest transition as the transition to the second Stark level of the $^2F_{5/2}$ multiplet, which is consistent with the assignment made in nearly all past work, with the remaining broad overlapping structure resulting from vibronic sidebands of the $1 \rightarrow 1$ transition. We attribute the overlapping peaks roughly 600 $cm^{-1}$ above the lowest transition as corresponding to the third Stark level. This interpretation agrees with the analysis of Refs. [16,21,23], while others have often assigned various weak components of the broad vibronic structure at lower energy as corresponding to the third level.

There have been fewer past studies of the energy level structure of the $^2F_{7/2}$ ground multiplet; emission spectra of $Yb^{3+}$:YAG have been reported down to liquid nitrogen temperature [18,24], but not at lower temperatures. Figure 2 shows a typical laser-excited fluorescence spectrum for emission from $^2F_{5/2}(1)$ at a temperature of $T = 4$ K. While only four transitions are expected from $^2F_{5/2}$ (1) to the four levels of the $^2F_{7/2}$ multiplet, the fluorescence spectrum is complicated by the appearance of broad bands and additional weak structure similar to what was observed in the absorption spectrum. We attribute the weak fluorescence structure observed from $\sim$300 $cm^{-1}$ to $\sim$500 $cm^{-1}$ as part of the vibronic sideband of the $1 \rightarrow 1$ emission line. Peak emission intensities to the second, third, and fourth levels of the $^2F_{7/2}$ multiplet occur at 9759 $cm^{-1}$,9171 $cm^{-1}$, and 9541 $cm^{-1}$, respectively, with the second and fourth levels being broadened and split presumably by near-resonant phonon coupling effects similar to those observed in the $^2F_{5/2}$ multiplet. From these values, we find that the upper levels of the $^2F_{7/2}$ multiplet are at 566 $cm^{-1}$,608 $cm^{-1}$, and 784 $cm^{-1}$ above the ground state. These values agree well with the results of Refs. [20,22].

### B. High-resolution laser-absorption spectrum of the $^2F_{7/2}(1) \rightarrow {}^2F_{5/2}(1)$ transition

For SHB and QIS applications, we are interested in the lowest to lowest $^2F_{7/2}(1) \rightarrow {}^2F_{5/2}(1)$ transition and its properties. The inhomogeneous linewidth is of particular interest because it can affect which QIS protocols can be implemented and what time-bandwidth products can be achieved in the contexts of optical signal processing. Figure 3 shows the laser-absorption spectrum of the $^2F_{7/2}(1) \rightarrow {}^2F_{5/2}(1)$ transition for 0.05% $Yb^{3+}$:YAG centered at 968.571 nm in vacuum at $T = 3.6$ K. The spectrum reveals an unusually sharp inhomogeneous line with a width of only 3.6 GHz (full width at half maximum

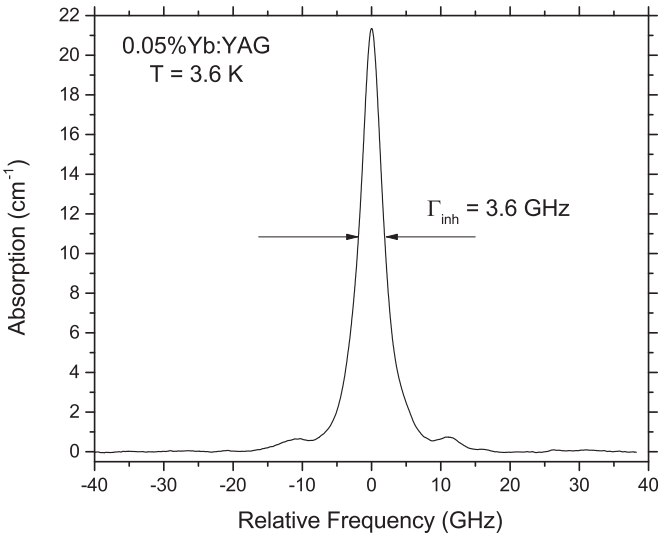


FIG. 3. Laser-absorption spectrum of the ${}^2F_{7/2} \rightarrow {}^2F_{5/2}$ transition at 968.571 nm (vacuum) in 0.05% $Yb^{3+}$:YAG at $T = 3.6$ K revealing an inhomogeneous linewidth of 3.6 GHz. Also noticeable in the spectrum are small satellite lines due to perturbed $Yb^{3+}$ sites in the crystal.

[FWHM]). Also noticeable in the spectrum are small satellite lines next to the main line. We expect that these satellite lines are due to perturbed $Yb^{3+}$ sites in the YAG lattice [33,34]. The inhomogeneous linewidth of 3.6 GHz, to the best of our knowledge, is almost an order of magnitude narrower than any other rare-earth-ion transition in YAG [3,39]. From the integrated absorption, we calculate a transition oscillator strength of $1.1 \times 10^{-6}$, a value that is at the upper end of the range observed for $4f$-$4f$ transitions of rare-earth ions in crystals.

### C. Characterization of the Zeeman effect

Zeeman splittings can dramatically affect spin dynamics when they are on the scale of the thermal energy $k_B T$. Hence, knowledge of the $g$-values in the ground and excited states is important. To reduce decoherence, the environmental $Yb^{3+}$ ions in the lattice surrounding the optically active ions should have large ground state $g$ factors to freeze out the spin population in the upper Zeeman level and hence reduce the spin flips that can cause spectral diffusion and decoherence. On the other hand, if Zeeman ground state sublevel storage is desired, the longest storage times are expected for small $g$-values and magnetic fields where the spin-flip rates are slower due to access to much lower acoustic phonon density of states.

Figure 4 compares absorption spectra for 0.05% $Yb^{3+}$:YAG at zero field and $T = 2$ K [Fig. 4(a)] with spectra for a magnetic field of $B = 4$ T parallel to ⟨111⟩ at temperatures of 10 K [Fig. 4(b)] and 2 K [Fig. 4(c)]. Please note that the spectral range in Fig. 4 is much larger than the spectral range in the laser-absorption scan of Fig. 3. The satellite lines observed in the laser-absorption scan of Fig. 3 are not fully resolved in the spectrometer scan and appear as shoulders on the main line of Fig. 4(a). Also clearly visible in the spectrum for zero field [Fig. 4(a)] are additional small satellite lines due

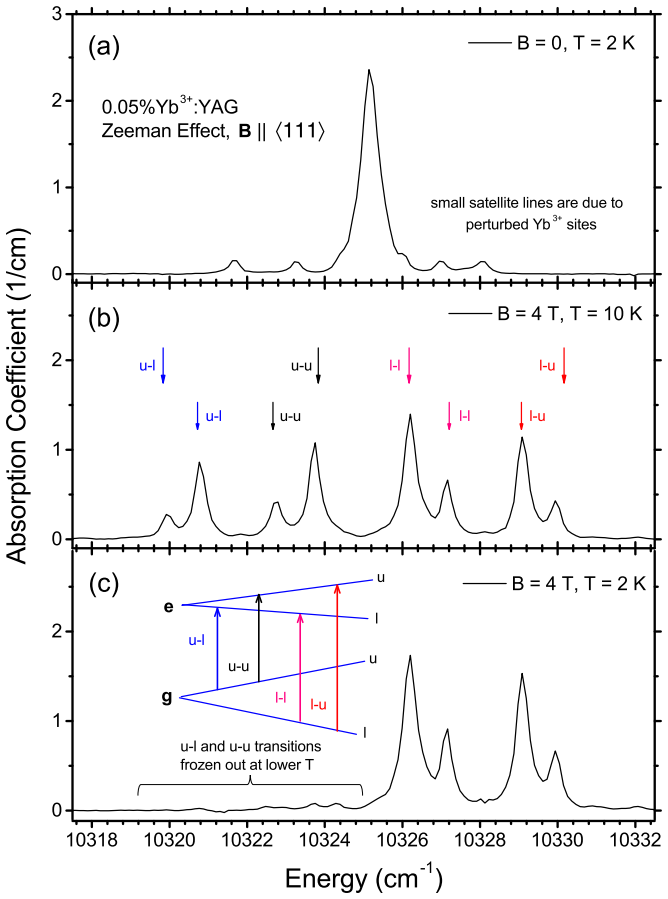


FIG. 4. Zeeman absorption spectra of the ${}^2F_{7/2}(1) \rightarrow {}^2F_{5/2}(1)$ transition for 0.05% $Yb^{3+}$:YAG: (a) at $T = 2$ K and zero field (small satellite lines are due to perturbed $Yb^{3+}$ sites); (b) at $T = 10$ K with $B = 4$ T oriented along ⟨111⟩, where two magnetically inequivalent subgroups of ions were identified and labeled with two sets of arrows (upper and lower) according to the transition labeling scheme in (c); (c) at $T = 10$ K with B = 4 T oriented along ⟨111⟩, where transitions originating from the higher energy level of the Zeeman-split ground state doublet are frozen out due to depopulation as the thermal energy is reduced to less than the Zeeman splitting.

to perturbed site transitions. As can be seen in Fig. 4(b), at a magnetic field of 4 T and $T = 10$ K, all Zeeman transitions are visible and well resolved. Two magnetically inequivalent subgroups of $Yb^{3+}$ ions give rise to two sets of transitions, as indicated by the two groups of arrows that follow the level and transition labeling scheme shown in Fig. 4(c). The magnetically inequivalent subgroup marked with the lower set of arrows has a ${}^2F_{7/2}$ ground state $g$-factor of 3.40 and a ${}^2F_{5/2}$ excited state $g$-factor of 1.04. The other subgroup marked with the raised set of arrows has a ground state $g$-factor of 3.34 and an excited state $g$-factor of 2.01. Figure 4(c) shows the corresponding Zeeman spectrum for $B = 4$ T at the lower temperature $T = 2$ K. Transitions originating from the upper level of the Zeeman-split ground state doublet for each subgroup are frozen out as the thermal energy is reduced to less than the Zeeman splitting, which was used to identify transitions.

Previous electron paramagnetic resonance (EPR) measurements by Carson and White gave ground state $g$-factors for $Yb^{3+}$ in YAG as $g_1 = 3.78$, $g_2 = 2.47$, and $g_z = 3.87$ [40]. However, these values were not associated with specific directions in the crystal. After comparing their convention of labeling to the spectrum of yttrium galium garnet (YGG) doped with $Yb^{3+}$ in their paper, in conjunction with the interpretation of Wolf *et al.* [41], we conclude that the $g_2 = 2.47$ direction was along ⟨001⟩. The other two $g$-factors correspond to the ⟨110⟩ directions. Wolf also surveyed the magnetic properties of $Yb^{3+}$ ions in aluminum garnets and measured the ground state $g$-values in $Yb^{3+}$:YAG as $g_x = 3.87$, $g_y = 3.78$, and $g_z = 2.47$ [42]. With these $g$-factors in mind, we find that the effective $g$-factors along the ⟨111⟩ direction should be

$$g_{\text{eff}} = \sqrt{\tfrac{2}{3}(3.78 \text{ or } 3.87)^2 + \tfrac{1}{3}(2.47)^2}, \tag{1}$$

predicting ground state $g$-factors of 3.47 and 3.40, which are very close to our measured values of 3.40 and 3.34. For coherent transient applications based on photon echoes, we are interested in the lower energy to lower energy transitions between the Zeeman sublevels. As can be inspected from Fig. 4(b), for both magnetically inequivalent subgroups, the transitions shift up in energy with the magnetic field along ⟨111⟩ with an effective $\Delta g$ of 1.2 and 0.67, respectively. The corresponding energy shift (frequency shift) of the lower to lower transition for both magnetically inequivalent sites is $0.56\,\text{cm}^{-1}\,\text{T}^{-1}$(17 GHz $\text{T}^{-1}$) and $0.31\,\text{cm}^{-1}\,\text{T}^{-1}$(9 GHz $\text{T}^{-1}$), respectively, and the site with the smaller shift has the higher transition probability.

### D. Thermal shift of the transition energy

The temperature dependence of the transition energy and linewidth is important in the context of optical frequency reference applications because it determines the thermal stability of the frequency reference obtained by locking lasers to spectral holes [43–48]. Lasers stabilized to spectral holes have recently become competitive with state-of-the-art cavity-stabilized systems and show great promise for achieving fractional frequency stabilities at the $10^{-17}$ level [49]. To investigate the thermal sensitivity of the ${}^2F_{7/2}(1) \rightarrow {}^2F_{5/2}(1)$ transition, we measured the center frequency and absorption linewidth over a large range of temperature from several Kelvin up to 300 K in the 0.05% $Yb^{3+}$:YAG sample. The measured thermal line shifts are shown by the symbols in Fig. 5, with the transition shifting by ∼160 GHz to lower frequency as the temperature increases from 4 K to 300 K. The thermal line shifts of all the absorption lines have been previously studied by Buchanan *et al.* over the limited temperature range of 80 K to 250 K, where the $1 \rightarrow 1$ transition exhibits an approximately linear temperature dependence [18]. Measurements from 80 K to higher temperatures of ∼410 K were carried out by Bogomolova *et al.*, revealing a slightly nonlinear dependence that was described using a simple model assuming coupling of resonant phonons to the lowest Stark levels of the ${}^2F_{7/2}$ and ${}^2F_{5/2}$ multiplets [20]. Since the thermal line shift becomes strongly nonlinear at lower temperatures, our results in Fig. 5 allow us to test the line shift models over a range where the dependence is much more sensitive to the values of the model parameters.

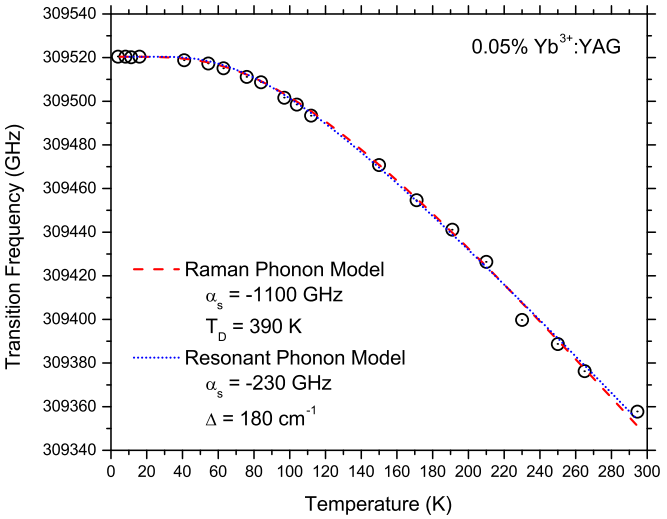


FIG. 5. Thermal line shift of the ${}^2F_{7/2} \rightarrow {}^2F_{5/2}$ transition frequency in 0.05% $Yb^{3+}$:YAG. The data were fit using the models described by Eqs. (2) and (3) with values for the resulting fit parameters shown.

The shift and broadening of spectral lines can be described by the effects of a combination of Raman scattering of nonresonant phonons from the ion and direct absorption or emission of phonons resonant with Stark level splittings within the ground or excited state multiplets [50,51]. If a Debye density of phonon states is assumed for the crystal, and the Raman scattering probability is assumed to be constant, then McCumber and Sturge found that the thermal shift of an optical transition due to the Raman two-phonon scattering process is described by

$$E(T) = E_0 + \alpha_s \left(\frac{T}{T_D}\right)^4 \int_0^{T_D/T} \frac{x^3}{e^x - 1} dx, \tag{2}$$

where $E_0$ is the transition energy at zero Kelvin, $T_D$ is the effective Debye temperature of the phonon modes that couple to the electronic states, and $\alpha_s$ is a coupling coefficient that describes the strength of the electron-phonon interaction [51]. For the case of the resonant phonon interaction, the simplest form of the energy shift may be derived by assuming that only phonons at a specific frequency $\Delta$ equal to an electronic energy level splitting couple to the electronic states. Using the general form of the interaction derived by Imbusch *et al.* [52], it is straightforward to show that under this assumption, the resulting energy shift is directly proportional to the thermal occupation of the resonant phonon mode, giving a dependence of

$$E(T) = E_0 + \frac{\alpha_s}{e^{\frac{\Delta}{kT}} - 1}. \tag{3}$$

Examining Eqs. (2) and (3), we see that both line shift processes exhibit a linear temperature dependence at higher temperatures, while at very low temperatures, the Raman process varies as $T^4$, and the resonant phonon process exhibits an Arrhenius-type exponential activation.

In a majority of past work on rare-earth-ion transitions in crystals, observed thermal line shifts have been described using Eq. (2) (see, for example, Refs. [53–55]). In contrast, past work by Bogomolova *et al.* found that the shift for $Yb^{3+}$:YAG was well described by Eq. (3) assuming a phonon energy of $\Delta = 400\,cm^{-1}$ [20]. In Fig. 5, we compare fits using Eq. (2) and Eq. (3), separately, to our measurements, allowing $\alpha_s$, $T_D$, and $\Delta$ to vary in the fitting process, with the parameter values given in the figure. The two models give comparable agreement with the experimental data over the entire temperature range. To describe the observed shift with the Raman process requires a relatively low Debye temperature of 390 K, which is smaller than the actual value of ∼500 K reported for rare-earth-doped YAG [56]. A reduced "effective" Debye temperature is often required to describe thermal line shifts and linewidths, an effect indicating that the rare-earth-ion states preferentially couple to the lower frequency phonon modes. For the resonant process, a phonon energy of $180\,cm^{-1}$ is required to describe the low-temperature behavior; this value is significantly lower than the value used in Ref. [20] to describe the nearly linear behavior at high temperatures. While the effective phonon energy is also much smaller than the actual $^2F_{5/2}$ Stark splitting of $\sim 300\,cm^{-1}$, it is known that the effect of averaging over a broadened distribution of energy splittings causes the "effective" energy determined by fitting observed data to be significantly reduced below the center of gravity of the splitting [57], potentially explaining the value in this case. Consequently, there is no conclusive indication of whether the Raman or resonant phonon model is the correct interpretation of the line shift in this case. An even more sensitive measurement technique such as SHB could determine the functional form of the line shift at the lowest temperatures where the models should be discernible [55].

For the purpose of comparing the thermal stability of the transition frequency to other SHB frequency reference materials, we consider the fit of the Raman phonon model at low temperatures where the line shift is proportional to $T^4$ [55]. Using the fitting results shown in Fig. 5, we find that the corresponding thermal sensitivity for this transition in $Yb^{3+}$:YAG is $310\,Hz\,K^{-4}$, which is nearly the same as the line shifts of the $^7F_0$-$^5D_0$ transitions of both site 1 and site 2 of $Eu^{3+}$ : $Y_2SiO_5$ [55], the current leading SHB frequency reference material [46–49].

### E. Temperature dependence of the homogeneous linewidth

Decoherence due to interactions with thermally activated vibrational modes of the lattice is one of the primary limiting factors when storing and processing both classical and quantum information in solid-state materials. While these perturbations can be strongly suppressed by operating at liquid helium temperatures, the thermally driven dynamics can still limit coherence lifetimes. Consequently, it is essential to understand the interactions driving thermal decoherence and the corresponding increase in homogeneous linewidth with temperature. Because broadening mechanisms exhibit different characteristic temperature dependencies, studying the variation in homogeneous linewidth over a wide range of temperatures can provide insight into the dominant sources of optical decoherence at low temperatures.

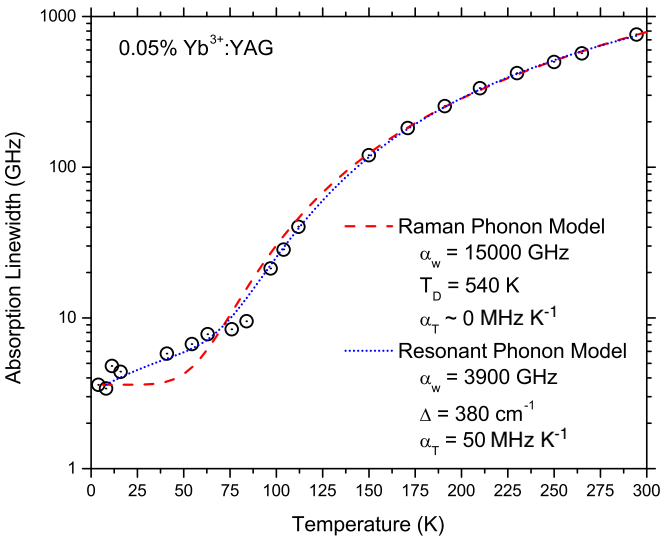


FIG. 6. Thermal broadening of the inhomogeneous line of the $^2F_{7/2} \rightarrow {}^2F_{5/2}$ transition in 0.05% $Yb^{3+}$:YAG. The data were fit using the models described by Eqs. (4) and (5) with values for the resulting fit parameters shown.

As can be observed from the absorption and fluorescence spectra in Figs. 1 and 2, the Stark levels in the ground and excited states are separated by very large gaps of hundreds of wavenumbers in $Yb^{3+}$:YAG, which are unusually large values for rare-earth ions in crystals. The relative energies of these levels determine the energies of the resonant phonons required to couple the electronic levels and therefore strongly influence the thermal decoherence and relaxation of both optical and spin transitions. The observation of this large isolation of the lowest levels in both the ground and excited multiplet suggests that the lowest to lowest $^2F_{7/2} \leftrightarrow {}^2F_{5/2}$ transition of $Yb^{3+}$ in YAG could potentially have interestingly reduced sensitivity to phonon-induced broadening caused by direct absorption and emission of phonons between crystal field levels [51,58].

Thermal broadening of the $^2F_{7/2} \leftrightarrow {}^2F_{5/2}$ transition has been previously studied over the temperature range from 80 K to 410 K by Bogomolova *et al.*, who modeled the temperature dependence as resulting from resonant phonon absorption at energies of $350\,cm^{-1}$ and $600\,cm^{-1}$ [20]. Figure 6 shows the results of our measurements of the absorption linewidth, revealing an increase from the inhomogeneously broadened limit of 3.6 GHz at 4 K to a homogeneous linewidth of ∼750 GHz at 300 K.

At temperatures above ∼80 K, we observe a rapid increase in linewidth that is characteristic of phonon interactions; however, at lower temperatures, the broadening exhibits an anomalous linear temperature dependence. It is known that broadening that is approximately linear with temperature can be present in some materials due to very low energy local vibrational modes that can be introduced by disorder and defects in the crystal structure. These dynamic disorder modes are often described using the theory of tunneling between states of local two-level systems (TLS) that was developed to describe the thermal properties of amorphous solids [59,60]. A low density of TLS modes may also appear in crystals if large random lattice strains are present [61], and homogeneous

broadening of rare-earth-ion transitions due to interactions with TLS modes has been observed experimentally in a number of crystals [62–64]. Furthermore, an increase in electronic spin-lattice relaxation rates has been observed in $Nd^{3+}$ : YAG crystals as the density of structural defects increases [65], an effect attributed to interaction with TLS modes, suggesting that disorder modes can be present in some YAG crystals.

To model the observed thermal broadening, we include contributions from phonon interactions as well as a linear temperature dependence with phenomenological coefficient $\alpha_T$ to describe any potential TLS interactions. If we assume that the dominant phonon interaction mechanism is nonresonant Raman scattering, we may use the theory of Ref. [51] to describe the temperature-dependent absorption linewidth as

$$\Gamma(T) = \Gamma_{\text{inh}} + \alpha_T T + \alpha_w \left(\frac{T}{T_D}\right)^7 \int_0^{T_D/T} \frac{x^6}{(e^x - 1)^2} dx, \quad (4)$$

where $\alpha_w$ is the phonon coupling constant, $T_D$ is the effective Debye temperature, and $\Gamma_{\text{inh}}$ is the contribution of inhomogeneous broadening to the absorption linewidth. Alternately, if we assume that homogeneous broadening arises from resonant phonon absorption to an electronic level at energy $\Delta$ above the ground or excited states involved in the transition, then the expected temperature dependence would be described by

$$\Gamma(T) = \Gamma_{\text{inh}} + \alpha_T T + \frac{\alpha_w}{e^{\frac{\Delta}{kT}} - 1}. \quad (5)$$

Examining Eqs. (4) and (5), we see that the Raman process exhibits a $T^7$ dependence at low temperatures and a $T^2$ dependence at high temperatures, while the resonant direct phonon process transitions from an Arrhenius-type exponential activation at low temperature to a linear dependence at high temperature. Fits of our data to these two models are shown in Fig. 6, where $\alpha_T$,$\alpha_w$,$T_D$, and $\Delta$ were allowed to vary, with the parameter values given in the figure. Both models give similar agreement at higher temperatures, but only the resonant phonon model correctly matches the data at low temperatures. In particular, inclusion of a nonzero linear term in the model to describe the low-temperature dependence prevents the Raman process from matching the data at higher temperatures, if the underlying linear dependence is assumed to hold over the entire temperature range. To describe the broadening at higher temperatures, the Raman process indicates a Debye temperature of 540 K that is very close to the known value for YAG [56]. In contrast to the results of Ref. [20], we find that the resonant phonon process describes the high-temperature broadening very well using only a single phonon energy of $380\,\text{cm}^{-1}$, which is comparable to the measured $^2F_{5/2}$ energy level splitting. The unusually large value of the direct phonon coupling coefficient obtained from this fit would suggest a homogeneous broadening of $\sim 130\,\text{cm}^{-1}$ for the 1-2 optical transition observed in the absorption spectrum shown in Fig. 1. While the transition does exhibit a width comparable to this value, the spontaneous phonon emission indicated by the fit of the resonant phonon model should produce a simple Lorentzian lineshape rather than the complex structure that is observed. Consequently, the large coupling coefficient could indicate that either the other electronic levels in the $^2F_{5/2}$ and $^2F_{7/2}$ multiplets contribute significantly to the direct phonon process or that the temperature dependence is produced by a combination of both the direct and Raman phonon scattering processes.

The linear broadening at low temperatures is described by a value of $\alpha_T = 50\,\text{MHz}\,\text{K}^{-1}$. This is a surprisingly large effect that is several orders of magnitude greater than what has been previously observed in high-quality crystals and is comparable to what is observed in highly disordered crystals or glasses, suggesting an unusually large density of TLS modes or an unusually large coupling strength between the TLS and $Yb^{3+}$, if that is indeed the mechanism responsible. Another mechanism that could potentially exhibit a linear temperature dependence would be direct phonon absorption and emission between the electronic spin states of the $Yb^{3+}$ or other paramagnetic impurities in the crystal; however, that mechanism would require the presence of a weak external magnetic field to become activated. Since the observed linear thermal broadening reaches several gigahertz at higher temperatures, the effects of unintentional paramagnetic impurities can be ruled out; an impurity density many orders of magnitude higher than the known purity of the crystal would be required to produce that level of broadening. To investigate the possibility of direct phonon interactions with the $Yb^{3+}$ electron spins themselves, we may derive the expected temperature dependence for a magnetic field of magnitude B interacting with the $Yb^{3+}$ magnetic moment described by an effective $g$-value of $g$. In the case of a weak stray field where the Zeeman splitting is much less than the thermal energy, the resulting temperature dependence is given by

$$\Delta\Gamma_h = \frac{\alpha_D g^2 B^4 k T}{2\pi \mu_B} = \alpha_T T, \quad (6)$$

where $\alpha_D$ is the direct phonon coupling coefficient, $k$ is the Boltzmann constant, and $\mu_B$ is the Bohr magneton. For our experimental conditions, we may place an upper limit of $\ll 10$ Gauss on any potential stray fields that might be present in the environment. Consequently, if we use the maximum $g$-value of 3.4 measured for $Yb^{3+}$ along $\langle 111 \rangle$ and assume a typical value for the direct phonon coupling coefficient of $\sim 1\,\text{Hz}/T^5$ as observed for other ions (see, for example, Ref. [66]), we find that the expected linear thermal broadening due to direct phonon interactions would be an exceedingly small $\ll 10^{-12}\,\text{Hz}\,\text{K}^{-1}$, indicating that that mechanism is far too weak to explain the observed broadening.

While interaction with TLS modes appears to be the most likely mechanism, no evidence for decoherence due to TLS was observed in our photon echo measurements, since linewidths on the order of kilohertz were observed at liquid helium temperatures, as discussed in later in section H. This indicates that, if present, the TLS modes must either fluctuate at rates significantly slower than the optical coherence lifetime at those temperatures, or they must be strongly suppressed by an applied magnetic field, such as the spin-elastic TLS modes that have been observed in erbium-doped glass [67]. Consequently, further measurements are required with applied magnetic fields and for different samples to unambiguously determine the source of the linear thermal broadening. If the linear broadening is shown to be due to TLS, we expect that new crystal growths or sample treatment (annealing, etc.) could

reduce or eliminate this contribution to the broadening. If we model the remaining phonon broadening as due to Raman scattering of phonons that has a $T^7$ dependence at low temperatures [55], the corresponding thermal broadening would only be $8 \times 10^{-4}$ Hz/K$^7$, which is significantly weaker than the broadening for leading quantum memory materials such as $Eu^{3+}$:YSO [55], $Eu^{3+}$:$Y_2O_3$ [68], and $Tm^{3+}$:YGG [69]. In either case, $Yb^{3+}$:YAG shows promise for reduced thermally induced decoherence if the anomalous linear component can be minimized.

### F. Fluorescence lifetime measurements

Spectral hole burning in $Yb^{3+}$:YAG takes place by population storage in the excited $^2F_{5/2}$ state; consequently, another important property that must be understood is the relaxation rate for the $Yb^{3+}$ $^2F_{5/2}$ excited state. The lifetime $T_1$ of the $^2F_{5/2}$ state also establishes an upper bound for the coherence lifetime $T_2$ via the relation $T_2 \leqslant 2T_1$. To determine the rate of relaxation of the $Yb^{3+}$ ions in the excited state, two measurement approaches were employed: the traditional fluorescence decay method and spectral hole lifetime measurements, as described in section G.

Figure 7 shows an example fluorescence decay in 1.5% $Yb^{3+}$:YAG at $T = 7$ K. In this experiment, a laser pulse was used to directly pump the lowest level of the excited state $^2F_{5/2}$ multiplet at 968.571 nm (vacuum), resulting in fluorescence to the individual levels of the $^2F_{7/2}$ ground state multiplet. Fluorescence intensity was recorded as a function of time with the photomultiplier while the spectrometer was tuned to the lowest level of the $^2F_{7/2}$ ground state multiplet. The fluorescence decay showed a single-exponential decay over several decades, fit to a fluorescence lifetime of $\tau_f = 1.0$ ms, as shown by the solid line in the figure. A slight increase in lifetime was observed by increasing the sample temperature to 75 K, 175 K, and room temperature. Increasing the $Yb^{3+}$ concentration to 10% and 20% also resulted in a slight increase of the measured lifetime. Our fluorescence decay measurements yielding ~1 ms lifetimes at 7 K agree well with the systematic temperature- and concentration-dependent measurements of Dong *et al.* [24]. However, a common problem with fluorescence decay measurements is radiative energy trapping, during which the emitted resonant photon is reabsorbed (trapped) and then re-emitted, slowing down the overall observed fluorescence decay and hence leading to apparent fluorescence lifetimes that are longer than the true excited state lifetime $T_1$ [70,71]. Radiative energy trapping has been reported for $Yb^{3+}$:YAG in the literature [24,70,72], and further evidence of it was observed in the dependence of the fluorescence lifetimes on the excitation geometry. Longer lifetimes were produced when the sample was excited towards the center of the crystal, and shorter lifetimes were produced when the sample was excited at the edge, indicating that the longer mean-free path when exciting at the center resulted in repeated photon absorption and re-emission events. To avoid the radiation trapping problem, time-resolved spectral hole decays described in the next section were measured.

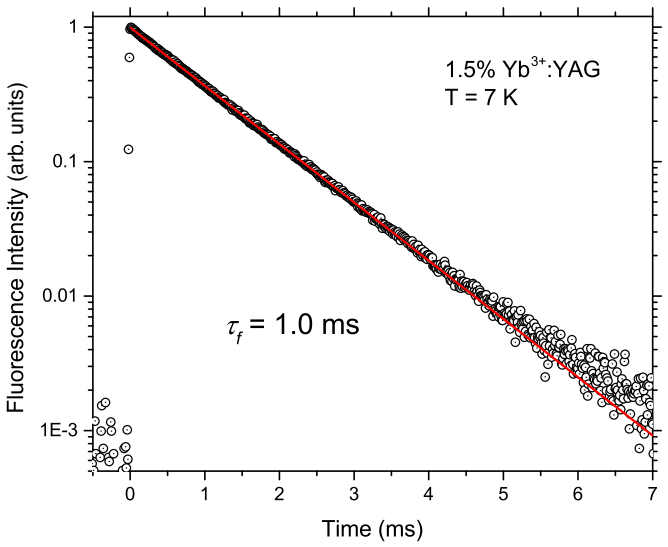


FIG. 7. Fluorescence lifetime decay of the $^2F_{7/2}(1) \rightarrow {}^2F_{5/2}(1)$ transition for 1.5% $Yb^{3+}$:YAG at $T = 7$ K. The solid line is a single-exponential fit to the data with a lifetime of $T_1 = 1.0$ ms showing good agreement.

### G. Spectral hole burning and spectral hole decay measurements

To obtain an accurate value for the $^2F_{5/2}$ excited state lifetime $T_1$, we applied time-resolved SHB to measure the population relaxation. Since the integrated absorption coefficient due to a spectral hole is directly proportional to the population difference between the $^2F_{7/2}$ and $^2F_{5/2}$ levels, the population dynamics can be unambiguously extracted from spectral hole decays. SHB minimizes radiation trapping and many other energy migration effects that often distort direct fluorescence measurements due to the very high spatial and spectral selectivity of the hole-burning process, generally providing a more reliable determination of the excited state lifetime for systems where hole-burning methods may be employed.

For SHB measurements, a small magnetic field of ~20 Gauss was applied along ⟨111⟩ with the sample at a temperature of $T = 2.8$ K to suppress spectral diffusion due to $Yb^{3+}$ spin flips by depopulating the ground state upper Zeeman sublevel. Spectral hole widths were ~8 MHz, and an example of a typical spectrum is shown in Fig. 8. Clearly visible are two sets of side holes around the main hole. The side holes are due to the transitions involving an electron spin flip driven simultaneously with the optical excitation. The side holes correspond to the excited state Zeeman splittings of $Yb^{3+}$ for the two magnetically inequivalent ions for this orientation. The magnitude of the splittings in comparison to the Zeeman experiments confirms a magnetic field strength of ~20 Gauss at the crystal. The hole widths did not vary significantly over the 50 $\mu$s to 3.5 ms measurement range, indicating that at this low magnetic field, the maximum spectral diffusion for timescales longer than 50 $\mu$s is <1 MHz and either occurs faster than 50 $\mu$s or is negligible compared to the homogeneous broadening. Detailed stimulated photon echo spectroscopy is needed to fully characterize the spectral diffusion in $Yb^{3+}$:YAG [66].

Time-resolved SHB measurements of the lowest $^2F_{5/2}$ state population relaxation were performed by recording the change

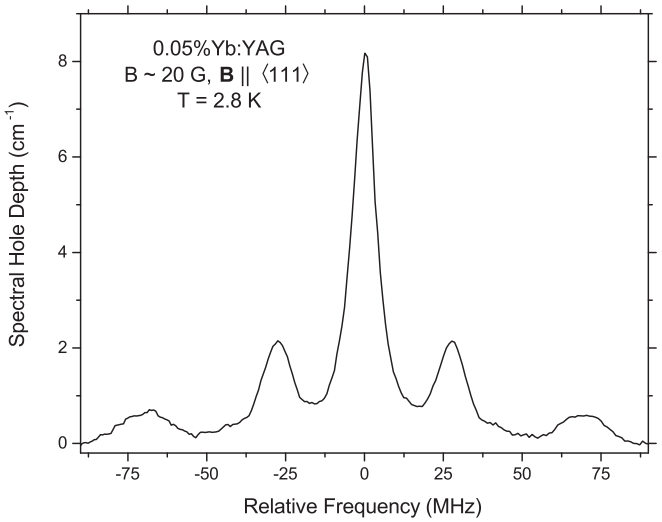


FIG. 8. Example of a spectral hole in 0.05% $Yb^{3+}$:YAG at 2.8 K with a field of ~20 Gauss along ⟨111⟩, showing strong electronic spin-flip sidebands.

in the integrated absorption coefficient due to the spectral hole. The entire spectral hole shape was scanned, eliminating detrimental effects arising from laser frequency jitter. Analysis of the decay of the spectral hole area allowed determination of the $^2F_{5/2}$ lifetime as shown in Fig. 9. The solid line in Fig. 9 is a single-exponential fit to the measured decay giving a spectral hole lifetime of 860 $\mu$s, which directly corresponds to the $^2F_{5/2}$ excited state $T_1$ lifetime. As expected, this result is noticeably shorter than the 1.0 ms value observed for the fluorescence decay, indicating the influence of radiation trapping in the fluorescence measurements.

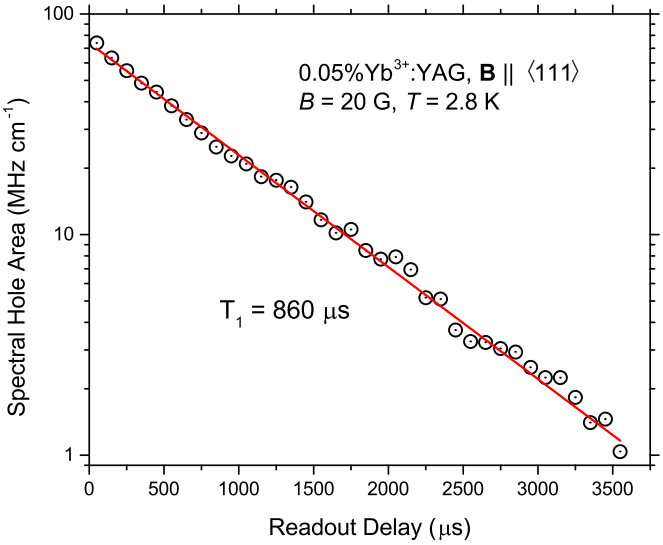


FIG. 9. Measured spectral hole decay in 0.05% $Yb^{3+}$:YAG at $T = 2.8$ K with a field of $B = 20$ Gauss along the ⟨111⟩ axis. The solid line is a single-exponential decay fit to the data showing good agreement and providing a $^2F_{5/2}(1)$ excited state lifetime of $T_1 = 860\,\mu$s.

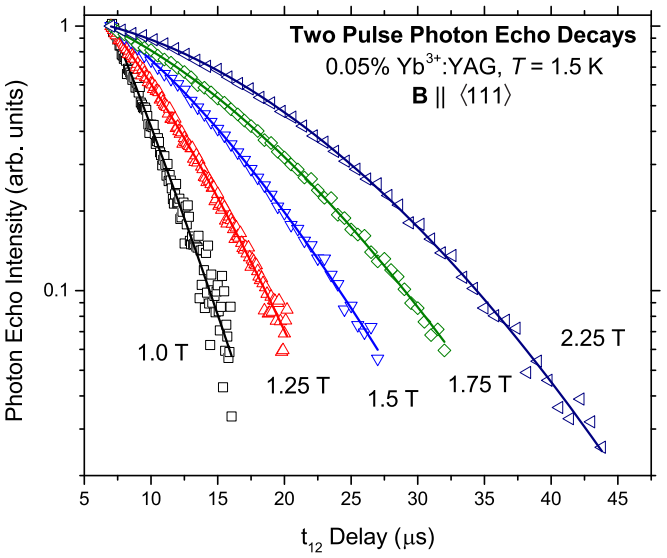


FIG. 10. Two-pulse photon echo decays in 0.05% $Yb^{3+}$:YAG at $T = 1.5$ K as a function of magnetic field strengths with B||⟨111⟩. Solid lines are fits of Eq. (7) to the data.

### H. Probing optical decoherence as a function of magnetic field strength

One of the most important properties for QIS and signal processing applications is the optical decoherence rate. To study decoherence in $Yb^{3+}$:YAG, two-pulse photon echo spectroscopy was used to overcome the resolution limits imposed by laser frequency jitter, power broadening, and time resolution typically found in techniques such as direct SHB measurements. The decays of two-pulse photon echoes as a function of magnetic field were measured at field strengths up to $B = 4$ T applied along ⟨111⟩ at a temperature of $T = 1.6$ K. The optical coherence is primarily affected by changes of the magnetic field, since it arises from long-range magnetic dipole-dipole interactions between the $Yb^{3+}$ ions in the lattice. Representative two-pulse photon echo decay curves for field strengths between $B = 1$ T and $B = 2.25$ T are plotted in Fig. 10. The decays were nonexponential, indicating the presence of spectral diffusion.

Spectral diffusion is a common phenomenon in this class of materials due to time-dependent frequency shifting interactions acting on the ions' transition frequencies. In the frequency domain, spectral diffusion causes the spectral hole to broaden over time, while in the time domain, it leads to a progressive increase in the rate of phase decoherence, which manifests itself in nonexponential decays [66,73,74]. To account for the effects of spectral diffusion on the photon echo decays, we used the empirical Mims function, describing the echo intensity $I$ as a function of pulse separation between pulse 1 and 2 as $t_{12}$, such that

$$I(t_{12}) = I_0 \exp\left\{-2\left(\frac{2t_{12}}{T_M}\right)^x\right\}, \tag{7}$$

where the exponent $x$ determines the shape of the echo decay function, and $T_M$ is the phase memory time over which the material coherence decays to $1/e^2$ of the initial intensity $I_0$ or $1/e$ of the initial electric field amplitude [75,76]. The phase

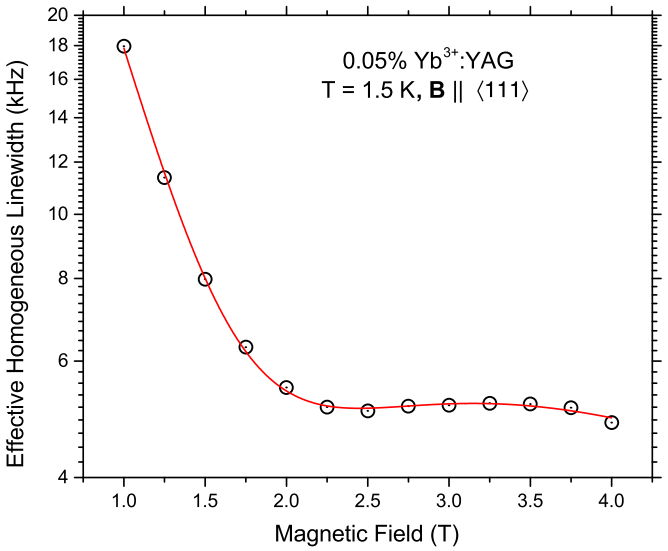


FIG. 11. Effective homogeneous linewidth dependence on magnetic field strength in 0.05% $Yb^{3+}$:YAG at 1.5 K with B||⟨111⟩. Symbols correspond to experimental data. The solid line is a fit to the spectral diffusion model described by Eqs. (8)–(10).

memory time $T_M$ in turn may be used to define an "effective" homogeneous linewidth (or decoherence rate) as

$$\Gamma_h = \frac{1}{\pi T_M}, \tag{8}$$

in analogy to the definition of the homogeneous linewidth from $T_2$ in the case where spectral diffusion is absent. Effective homogenous linewidths according to Eq. (8) were extracted from two-pulse photon echo decays as a function of magnetic field and are plotted in Fig. 11. An effective homogeneous linewidth of ∼18 kHz was obtained for a magnetic field of $B = 1$ T. Increasing the magnetic field strength suppresses the effective homogeneous linewidth to 5.0 kHz at $B = 2.5$ T. Further increases in field strength cause a small "bump" where the effective homogeneous linewidth increases to 5.2 kHz at 3.25 T before it then decreases to 4.8 kHz at 4 T.

The general magnetic field behavior exhibited in Fig. 11 has been observed in other paramagnetic rare-earth materials and is a general feature of spectral diffusion caused by phonon-driven electron spin flips [74,77–79]. The local maximum in the magnetic field dependence of the effective homogeneous linewidth can be quantitatively predicted based on the magnetic dipole-dipole interactions between $Yb^{3+}$ ions. When an $Yb^{3+}$ ion spin changes its orientation, it causes a small shift in the magnetic field strength for all other $Yb^{3+}$ ions in its environment and hence slightly shifts their transition frequencies by a random amount that depends on their relative position in the crystal. These dynamic perturbations lead to the spectral diffusion that is reflected in the nonexponential echo decay shapes. Following our previous spectral diffusion analysis, the observed variation of the effective homogeneous linewidth with magnetic field can be described by the interplay of two parameters: the spectral diffusion linewidth,$\Gamma_{SD}$, and the spectral diffusion rate, $R$, which have opposing magnetic field dependencies [66,74]. The spectral diffusion linewidth rapidly decreases with magnetic field strength as the thermal population of the upper ground state Zeeman component is frozen out. On the other hand, the rate of spectral diffusion given by the sum of the upward and downward spin-flip transition rates of the perturbing spins can increase with magnetic field, since the energy splitting accesses a larger density of states of resonant phonons at higher energies. In addition to this mechanism, electron spin flips may also be driven directly by the dipole-dipole interaction between spins, leading to rapid "flip-flops" of resonant antiparallel electron spin pairs in the crystal. Because the flip-flop process requires two antiparallel spins, it is strongly suppressed as the higher energy spin state is depopulated with increasing magnetic field strength. In addition to these effects, several other field-independent or weakly field-dependent mechanisms can also contribute to spectral diffusion [66].

Following the analysis of spectral diffusion developed for $Er^{3+}$:$Y_2SiO_5$ [66], $Er^{3+}$:$LiNbO_3$ [79], and $Er^{3+}$:KTP [74], we can quantitatively model the magnetic field dependence by considering the influence of $R$ and $\Gamma_{SD}$ on the phase decoherence time $T_M$ of two-pulse echo decays, which is given by

$$T_M = \frac{2\Gamma_0}{\Gamma_{SD} R} \cdot \left( -1 + \sqrt{1 + \frac{\Gamma_{SD} R}{\pi \Gamma_0^2}} \right), \tag{9}$$

where $\Gamma_0$ is the homogeneous linewidth in the absence of spectral diffusion. Although two-pulse photon echo decays do not contain enough information to separate the spectral diffusion magnitude and rate, which would require more elaborate stimulated photon echo measurements [66], we can still model the spectral diffusion using the dependence of the product $\Gamma_{SD} R$ that appears in Eq. (9) [74]. With this approach, the resulting magnetic field dependence is described by

$$\Gamma_{SD} R = \left[ a_D g^3 B^5 \coth\left(\frac{g\mu_B B}{2kT}\right) + b_F g^4 \mathrm{sech}^2\left(\frac{g\mu_B B}{2kT}\right) + c_0 \right] \cdot \mathrm{sech}^2\left(\frac{g\mu_B B}{2kT}\right), \tag{10}$$

where $a_D$,$b_F$, and $c_0$ are parameters that describe the relative influence of the direct phonon process, spin flip-flops, and other field-independent mechanisms, respectively. The dependence given by Eq. (10) may then be combined with Eq. (9) and Eq. (8) to model the observed magnetic field dependence of the coherence lifetime or homogeneous linewidth. The fit of this model to our data for $Yb^{3+}$:YAG is shown in Fig. 11 by the solid line, giving excellent agreement using the measured values of $T = 1.5$ K and $g = 3.4$ in the model. Since we expect the field-independent effects to be small at this low temperature, we have also set $c_0 = 0$ so that $a_D$,$b_F$, and $\Gamma_0$ are the only model parameters allowed to vary in the fitting process, giving values of 280 $kHz^2/T^5$,1.8 × $10^6 kHz^2$, and 2.9 kHz, respectively. Consequently, we find that our model for decoherence caused by $Yb^{3+}$-$Yb^{3+}$ magnetic dipole interactions successfully describes the observed behavior in this system.

## V. CONCLUSIONS

The results presented in this paper provide an initial overview of the spectroscopic, decoherence, and SHB properties of $Yb^{3+}$:YAG relevant for SHB and QIS applications at a wavelength of 968 nm. This material system exhibits a number of desirable properties such as a large transition dipole moment (relative to other $4f$-$4f$ transitions), large Stark splittings in both the ground and excited state multiplets, a convenient laser-accessible wavelength, and an inhomogeneous bandwidth well matched to many applications. The decoherence dynamics exhibit behavior that is comparable to other paramagnetic ions, such as $Nd^{3+}$ and $Er^{3+}$, that are used in quantum information and photonics demonstrations, with homogeneous linewidths of a few kilohertz achievable using field strengths low enough to be generated by simple permanent magnet arrangements. The temperature dependence of the homogeneous linewidth indicates a phonon coupling that is weaker than other leading $Eu^{3+}$ and $Tm^{3+}$ material systems; however, a strong linear temperature dependence characteristic of slow glassy dynamics is observed at low temperatures, limiting the benefit of the weak phonon coupling. Consequently, additional comprehensive studies of all these properties as a function of magnetic field strength and orientation, temperature, and $Yb^{3+}$ concentration will be required to determine the source of this anomalous temperature dependence and whether it may be minimized by improved crystal growth or annealing methods. Overall, our results show that $Yb^{3+}$:YAG is a suitable material system for many photonic and QIS applications, and it offers a promising combination of properties with distinct differences from other known SHB materials.

## ACKNOWLEDGMENTS

T.B. wishes to acknowledge financial support from the University of San Francisco Faculty Development Fund. This material is based in part on work supported by the National Science Foundation (NSF) under Awards No. PHY-1415628 and No. CHE-1416454 and the Montana Research and Economic Development Initiative (MREDI).

[1] W. Tittel, M. Afzelius, T. Chaneliére, R. L. Cone, S. Kröll, S. A. Moiseev, and M. Sellars, Laser and Photon. Rev. **4**, 244 (2010).
[2] C. Simon, M. Afzelius, J. Appel, A. B. de la Giroday, S. J. Dewhurst, N. Gisin, C. Hu, F. Jelezko, S. Kröll, J. H. Müller, J. Nunn, E. Polzik, J. Rarity, H. de Riedmatten, W. Rosenfeld, A. J. Shields, N. Sköld, R. M. Stevenson, R. Thew, I. Walmsley, M. Weber, H. Weinfurter, J. Wrachtrup, and R. J. Young, Eur. Phys. J. D **58**, 1 (2010).
[3] C. W. Thiel, T. Böttger, and R. L. Cone, J. Lumin. **131**, 353 (2011).
[4] W. R. Babbitt, Z. W. Barber, S. H. Bekker, M. D. Chase, C. Harrington, K. D. Merkel, R. K. Mohan, T. Sharpe, C. R. Stiffler, A. S. Traxinger, and A. J. Woidtke, Laser Phys. **24**, 094002 (2014).
[5] Z. Kis, G. Mandula, K. Lengyel, I. Hajdara, L. Kovacs, and M. Imlau, Opt. Mater. **37**, 845 (2014).
[6] P. Lacovara, H. K. Choi, C. A. Wang, R. L. Aggarwal, and T. Y. Fan, Opt. Lett. **16**, 1089 (1991).
[7] W. F. Krupke, Curr. Opin. Sol. State Mat. Sci. **4**, 197 (1999).
[8] E. Innerhofer, T. Südmeyer, F. Brunner, R. Häring, A. Aschwanden, R. Paschotta, C. Hönninger, M. Kumkar, and U. Keller, Opt. Lett. **28**, 367 (2003).
[9] D. S. Sumida, A. A. Betin, H. Bruesselbach, R. B. Matthews, R. Q. Reeder, and M. S. Mangir, Laser Focus World **63**, 67 (1999).
[10] C. Wandt, S. Klingebiel, S. Keppler, M. Hornung, M. Loeser, M. Siebold, C. Skrobol, A. Kessel, S. A. Trushin, Z. Major, J. Hein, M. C. Kaluza, F. Krausz, and S. Karsch, Laser and Photon. Rev. **8**, 875 (2014).
[11] E. Saglamyurek, N. Sinclair, J. Jin, J. A. Slater, D. Oblak, F. Bussières, M. George, R. Ricken, W. Sohler, and W. Tittel, Nature **469**, 512 (2011).
[12] C. W. Thiel, N. Sinclair, W. Tittel, and R. L. Cone, Phys. Rev. Lett. **113**, 160501 (2014).
[13] T. Zhong, J. M. Kindem, E. Miyazono, and A. Faraon, Nat. Commun. **6**, 8206 (2015).
[14] L. A. Williamson, Y.-H. Chen, and J. J. Longdell, Phys. Rev. Lett. **113**, 203601 (2014).
[15] C. O'Brien, N. Lauk, S. Blum, G. Morigi, and M. Fleischhauer, Phys. Rev. Lett. **113**, 063603 (2014).
[16] D. L. Wood, J. Chem. Phys. **39**, 1671 (1963).
[17] J. A. Koningstein, Teor. Chim. Acta **3**, 271 (1965).
[18] R. A. Buchanan, K. A. Wickersheim, J. J. Pearson, and G. F. Herrmann, Phys. Rev. **159**, 245 (1967).
[19] J. J. Pearson, G. F. Herrmann, K. A. Wickersheim, and R. A. Buchanan, Phys. Rev. **159**, 251 (1967).
[20] G. A. Bogomolova, D. N. Vylegzhanin, and A. A. Kaminskii, Sov. Phys. JETP **42**, 440 (1976).
[21] G. A. Bogomolova, L. A. Bumagina, A. A. Kaminskii, and B. Z. Malkin, Sov. Solid State Phys. **19**, 1439 (1977).
[22] A. A. Kaminskii, *Laser Crystals* (Springer, Berlin, 1981), p. 146.
[23] A. Lupei, V. Enaki, V. Lupei, C. Presura, and A. Petraru, J. Alloy. Compd. **275-277**, 196 (1998).
[24] J. Dong, M. Bass, Y. Mao, P. Deng, and F. Gan, J. Opt. Soc. Amer. B **20**, 1975 (2003).
[25] D. C. Brown, R. L. Cone, Y. Sun, and R. W. Equall, IEEE J. Sel. Topics Quant. Electron. **11**, 604 (2005).
[26] G. Menzer, Z. Krist. **63**, 157 (1926).
[27] S. Geller, Z. Krist. **125**, 1 (1967).
[28] C. B. Rubinstein and R. L. Barns, Amer. Mineral. **49**, 1489 (1964).
[29] F. Euler and J. A. Bruce, Acta Crystallogr. **19**, 971 (1965).
[30] R. D. Shannon, Acta Crystallogr. A **32**, 751 (1976).
[31] J. Dong and K. Lu, Phys. Rev. B **43**, 8808 (1991).
[32] V. Lupei, G. Boulon, and A. Lupei, J. Phys.: Condens. Matter **5**, L35 (1993).
[33] G. Wang, Defect and coherent transient optical spectroscopy of rare earth doped crystals, Doctoral Dissertation, Montana State University, Bozeman, Montana, 1997.
[34] G. D. Reinemer, Optical characterization of perturbed sites and $C_{3i}$ sites in rare earth doped oxide crystals, Doctoral Dissertation, Montana State University, Bozeman, Montana, 2003.

[35] M. Kreye and K. D. Becker, Phys. Chem. Chem. Phys. **5**, 2283 (2003).
[36] I. Mills, T. Cvitas, K. Homann, N. Kallay, and K. Kuchitsu, *Quantities, Units and Symbols in Physical Chemistry* (Blackwell Scientific Publications, Oxford, UK, 1988).
[37] M. Dahl and G. Schaack, J. Lumin. **31-32**, 84 (1984).
[38] A. Lupei, V. Lupei, C. Presura, V. N. Enaki, and A. Petraru, J. Phys.: Cond. Matter **11**, 3769 (1999).
[39] R. M. Macfarlane, Opt. Lett. **18**, 829 (1993).
[40] J. W. Carson and R. L. White, J. Appl. Phys. **31**, S53 (1960).
[41] W. P. Wolf, M. Ball, M. T. Hutchings, M. J. M. Leask, and A. F. G. Wyatt, J. Phys. Soc. Japan **17**, Suppl. B-1, 443 (1962).
[42] M. Ball, G. Garton, M. J. M. Leask, D. Ryan, and W. P. Wolf, J. Appl. Phys. **32**, S267 (1961).
[43] P. B. Sellin, N. M. Strickland, J. L. Carlsten, and R. L. Cone, Opt. Lett. **24**, 1038 (1999).
[44] P. B. Sellin, N. M. Strickland, T. Böttger, J. L. Carlsten, and R. L. Cone, Phys. Rev. B **63**, 155111 (2001).
[45] T. Böttger, G. J. Pryde, C. W. Thiel, and R. L. Cone, J. Lumin. **127**, 83 (2007).
[46] M. J. Thorpe, L. Rippe, T. M. Fortier, M. S. Kirchner, and T. Rosenband, Nat. Photonics **5**, 688 (2011).
[47] Q. F. Chen, A. Troshyn, I. Ernsting, S. Kayser, S. Vasilyev, A. Nevsky, and S. Schiller, Phys. Rev. Lett. **107**, 223202 (2011).
[48] M. J. Thorpe, D. R. Leibrandt, and T. Rosenband, New J. Phys. **15**, 033006 (2013).
[49] S. Cook, T. Rosenband, and D. R. Leibrandt, Phys. Rev. Lett. **114**, 253902 (2015).
[50] J. H. Van Vleck, Phys. Rev. **57**, 426 (1940).
[51] D. E. McCumber and M. D. Sturge, J. Appl. Phys. **34**, 1682 (1963).
[52] G. F. Imbusch, W. M. Yen, A. L. Schawlow, D. E. McCumber, and M. D. Sturge, Phys. Rev. **133**, A1029 (1964).
[53] W. M. Yen, W. C. Scott, and A. L. Schawlow, Phys. Rev. **136**, A271 (1964).
[54] T. Kushida, Phys. Rev. **185**, 500 (1969).
[55] F. Könz, Y. Sun, C. W. Thiel, R. L. Cone, R. W. Equall, R. L. Hutcheson, and R. M. Macfarlane, Phys. Rev. B **68**, 085109 (2003).
[56] M. G. Beghi, C. E. Bottani, and V. Russo, J. Appl. Phys. **87**, 1769 (2000).
[57] B. A. Young and H. J. Stapleton, Phys. Lett. **21**, 498 (1966).
[58] R. Orbach and H. J. Stapleton, in *Electron Paramagnetic Resonance*, edited by S. Geschwind (Plenum, New York, 1972), p. 121.
[59] P. W. Anderson, B. I. Halperin, and C. M. Varma, Phil. Mag. **25**, 1 (1972).
[60] W. A. Phillips, J. Low Temp. Phys. **7**, 351 (1972).
[61] S. K. Watson, Phys. Rev. Lett. **75**, 1965 (1995).
[62] G. P. Flinn, K. W. Jang, J. Ganem, M. L. Jones, R. S. Meltzer, and R. M. Macfarlane, Phys. Rev. B **49**, 5821 (1994).
[63] R. S. Meltzer, K. W. Jang, K. S. Hong, Y. Sun, and S. P. Feofilov, J. Alloys Compd. **250**, 279 (1997).
[64] R. M. Macfarlane, Y. Sun, R. L. Cone, C. W. Thiel, and R. W. Equall, J. Lumin. **107**, 310 (2004).
[65] L. K. Aminov, I. N. Kurkin, and D. A. Lukoyanov, Appl. Magn. Reson. **14**, 447 (1998).
[66] T. Böttger, C. W. Thiel, Y. Sun, and R. L. Cone, Phys. Rev. B **73**, 075101 (2006).
[67] R. M. Macfarlane, Y. Sun, P. B. Sellin, and R. L. Cone, Phys. Rev. Lett. **96**, 033602 (2006).
[68] W. R. Babbitt, A. Lezama, and T. W. Mossberg, Phys. Rev. B **39**, 1987 (1989).
[69] C. W. Thiel, N. Sinclair, W. Tittel, and R. L. Cone, Phys. Rev. B **90**, 214301 (2014).
[70] D. S. Sumida and T. Y. Fan, Opt. Lett. **19**, 1343 (1994).
[71] J. A. Muñoz, B. Herreros, G. Lifante, and F. Cussó, Phys. Status Solidi (a) **168**, 525 (1998).
[72] F. D. Patel, E. C. Honea, J. Speth, S. A. Payne, R. Hutcheson, and R. Equall, IEEE J. Quant. Electron. **37**, 135 (2001).
[73] T. Böttger, C. W. Thiel, R. L. Cone, and Y. Sun, Phys. Rev. B **79**, 115104 (2009).
[74] T. Böttger, C. W. Thiel, Y. Sun, and R. L. Cone, J. Lumin. **169**, 466 (2016).
[75] W. B. Mims, Phys. Rev. **168**, 370 (1968).
[76] W. B. Mims, in *Electron Paramagnetic Resonance*, edited by S. Geschwind (Plenum Press, New York, 1972), Chap. 4.
[77] R. M. Macfarlane, T. L. Harris, Y. Sun, R. L. Cone, and R. W. Equall, Opt. Lett. **22**, 871 (1997).
[78] Y. Sun, R. L. Cone, L. Bigot, and B. Jacquier, Opt. Lett. **31**, 3453 (2006).
[79] C. W. Thiel, R. M. Macfarlane, T. Böttger, Y. Sun, R. L. Cone, and W. R. Babbitt, J. Lumin. **130**, 1603 (2010).